Journal of
Synchrotron Radiation

ISSN 0909-0495

Received 3 July 2008
Accepted 23 December 2008

High-resolution spectroscopy on an X-ray absorption beamline

Jean-Louis Hazemann,[a]* Olivier Proux,[b] Vivian Nassif,[c] Hervé Palancher,[d] Eric Lahera,[b] Cécile Da Silva,[a] Aurélien Braillard,[a] Denis Testemale,[a] Marie-Ange Diot,[a] Isabelle Alliot,[c] William Del Net,[b] Alain Manceau,[b] Frédéric Gélébart,[e] Marc Morand,[e] Quentin Dermigny[e] and Abhay Shukla[e]

[a]Institut Néel, CNRS, 25 avenue des Martyrs, 38042 Grenoble Cedex 9, France, [b]Laboratoire de Géophysique Interne et Tectonophysique, UMR CNRS - Université Joseph Fourier, 1381 rue de la Piscine, Domaine Universitaire, 38400 Saint-Martin-d'Hères, France, [c]CEA/Grenoble, DRFMC/SP2M/NRS, 17 avenue des Martyrs, 38054 Grenoble Cedex 9, France, [d]CEA-Cadarache, Department for Nuclear Fuel Study, 13108 Saint Paul lez Durance, France, and [e]Institut de Minéralogie et de Physique des Milieux Condensés, Université Paris 6, Université Paris 7, CNRS, IPGP, Case 115, 4 Place Jussieu, 75252 Paris Cedex 05, France.
E-mail: jean-louis.hazemann@grenoble.cnrs.fr

A bent-crystal spectrometer based on the Rowland circle geometry has been installed and tested on the BM30b/FAME beamline at the European Synchrotron Radiation Facility to improve its performances. The energy resolution of the spectrometer allows different kinds of measurements to be performed, including X-ray absorption spectroscopy, resonant inelastic X-ray scattering and X-ray Raman scattering experiments. The simplicity of the experimental device makes it easily implemented on a classical X-ray absorption beamline. This improvement in the fluorescence detection is of particular importance when the probed element is embedded in a complex and/or heavy matrix, for example in environmental sciences.

Keywords: X-ray absorption spectroscopy; high-resolution X-ray analyzer; inelastic X-ray scattering; bent crystal.

1. Introduction

The CRG-FAME (French absorption spectroscopy beamline in material and environmental sciences) beamline at the European Synchrotron Radiation Facility (ESRF, Grenoble, France) is dedicated to X-ray absorption spectroscopy (XAS). Open to users since September 2002, FAME covers a wide variety of common applications of XAS in condensed matter physics, materials science, biophysics, chemistry and mainly in geochemical sciences (more than 50% of the beam time).

In most cases the probed elements are highly diluted. FAME being a bending-magnet beamline, the design of the optical elements has been performed firstly to maximize the photon flux on the sample and secondly to optimize the beamline stability and reduce the non-statistical noise (Proux *et al.*, 2005, 2006). Moreover, for an optimal acquisition of XAS spectra in such highly diluted conditions, the intense X-ray beam on the sample needs to be associated with a highly sensitive detection system. Fluorescence detection is currently achieved with a 30-element Canberra Ge solid-state detector (SSD). To overcome mechanical limitations in the close packing of independent Ge elements, the SSD is based on an array of six Ge strips each containing five detection areas. With a 0.125 µs shaping time (highest counting rate), its average energy resolution is around 300 eV (full width at half-maximum, FWHM, like all the energy resolution numerical values given in this paper) as measured classically with a ^{55}Fe source (Mn $K\alpha$ peak, 5.9 keV). The maximum total input count rate accepted equals 80 kcounts s^{-1} element^{-1} without correction of dead-time. This detector is very efficient for the analysis of diluted elements but limitations do exist and are critical especially in earth science and geochemistry studies. Indeed, in these scientific fields, probed elements are often diluted and/or embedded in a complex matrix. The signal of interest is very often of the same order of magnitude as the background. Furthermore, in some cases, the fluorescence peaks of some matrix constituents can be too close in energy to the fluorescence peak of the targeted element to be discriminated by the SSD; for example, the $K\alpha$ fluorescence of a Z element and the $K\beta$ fluorescence of the $Z-1$ element overlap. One project of the beamline is thus to provide an alternative detector to overcome these difficulties, with a large counting rate and a largely improved energy resolution to discriminate the different fluorescence peaks.

New technologies can be used to improve the counting rate by multiplying the number of independent detection elements

with a detection area close to the total surface of the detection zone. An alternative to the SSD is the Ge pixel array detector (PAD). Recently, a 100-element PAD was developed (Oyanagi *et al.*, 2006). The characteristics obtained are similar to a Ge SSD. All included, the improvement of the total counting rate is around three with respect to the 30-element SSD but no improvement of the energy resolution is achieved.

Another way to improve the detection system is to use a crystal analyser which has a very good energy resolution coupled to a fast detector which has very large dynamics. Crystal analyzers in the transmission mode (bent-crystal Laue analyser, BCLA) are available (Zhong *et al.*, 1999; Khelashvili *et al.*, 2002; Kropf *et al.*, 2005). Their energy resolution is slightly better than a SSD, with a wide angular acceptance, but the absorption of the fluorescence signal through the silicon wafer restrains their use to rather high-energy experiments. In reflection mode this limitation is overcome. This geometry of detection is already used on bending magnet (BM) and insertion device (ID) spectroscopy beamlines (Goulon *et al.*, 2005; Welter *et al.*, 2005). The energy resolutions are greatly improved with respect to a SSD, ranging from below 0.2 eV at 8156 eV (Collart *et al.*, 2005) to around 6 eV at 9666 eV (Goulon *et al.*, 2005), depending on the radius of curvature of the bent crystals, the Bragg angle and the nature of the reflection.

For our purpose a crystal analyser spectrometer in reflection mode has been designed in the Johann geometry. Such a development will allow firstly an improvement of the quality in the 'classic' XAS spectra (i) by allowing the study of trace elements diluted in some particular matrix (partial fluorescence yield extended X-ray absorption fine structure, PFY-EXAFS) and (ii) by improving the energy resolution at the XAS edges (Hämäläinen *et al.*, 1991). Secondly, this spectrometer will provide the users with new tools for their spectroscopic analysis, resonant inelastic X-ray scattering (RIXS) (Kotani & Shin, 2001) and X-ray Raman scattering (XRS) (Bowron *et al.*, 2000). The state-of-the-art of all these spectroscopic techniques can be found in an exhaustive recent review (Schülke, 2007).

This kind of detection system is now used on dedicated ID inelastic scattering beamlines, *i.e.* using a high-flux beam (Bergmann & Cramer, 1998; Glatzel & Bergmann, 2005; Welter *et al.*, 2005; Goulon *et al.*, 2005; Huatari *et al.*, 2006). The main aim is to implement such instrumentation on a classical BM XAS beamline. In this paper we will present briefly the performances of the beamline (§2), the experimental conditions (§3) and the preliminary experiments and results obtained with a crystal analyser apparatus (§4).

2. Beamline performances

2.1. Optics

The design of the beamline was carried out in order to (i) accept the full fan (3 mrad) delivered by the 0.8 T BM of the ESRF storage ring, (ii) have the maximum flux on the sample and (iii) ensure an optimal stability (Proux *et al.*, 2005, 2006). A two-crystal monochromator is placed between two Rh-coated mirrors. The incidence angle of both mirrors can be adjusted to precisely adapt the critical energy for each probed edge. Their cylindrical shapes can be precisely adjusted for each incidence angle in order to optimize their focusing properties. The first mirror allows a beam collimation (source to infinity focusing) on the cryogenically cooled first silicon (220) crystal of the monochromator. The second mirror vertically focuses the beam on the sample. The second crystal of the monochromator is sagittally and dynamically bent to focus horizontally the beam on the sample for each energy (Hazemann *et al.*, 1995). The automatic angular feedback of the angle between the two Si(220) crystals leads to a permanent optimization of the monochromatic beam intensity during an energy scan (in the step-by-step or continuous quick-scan mode). To perform this tuning, the second crystal oscillates continuously at 440 Hz with maximum amplitude around 0.1 µrad. The height of the exit beam is variable after the monochromator, the gap between the two crystals being kept constant. The vertical position of the experimental table is then adjusted dynamically during an energy scan to follow exactly the height of the beam.

With these optical characteristics the size of the beam on the sample is kept constant during an energy scan at around 300×200 µm (horizontal $\times$ vertical, FWHM). The beam stability on the sample in the vertical and horizontal position is ± 2 µm during a 1 keV scan. The energy resolution of the incident beam is close to the theoretical value given by the Darwin width of the two Si(220) reflections, thanks to the white beam collimation by the first mirror and to the lack of thermal distortion on the first monochromator crystal. This last point is important for X-ray absorption near-edge structure (XANES) studies, especially when the experimental spectra are compared with theoretical calculations (D'Angelo *et al.*, 2005; Arcovito *et al.*, 2005; Titov *et al.*, 2005).

2.2. Sample concentration limit

In the environmental and earth science fields, two main factors can limit the ability to perform EXAFS experiments under optimal conditions: (i) the dilution of the probed trace elements and/or (ii) the nature of the matrix. When the probed element is diluted in a light matrix, the intensity of the collected signal by the fluorescence detector is exclusively due to the photon flux on the sample and to the amount of the absorbing element. When the probed element is diluted in a heavy matrix (such as iron or manganese oxides, for example), the fluorescence signals delivered by the main constituents of this matrix can saturate the detectors, even with the use of appropriate filters.

To quantify the sensitivity of the beamline, we collected the concentration limits published from experiments performed on FAME from these two scientific fields (Fig. 1). In all cases the fluorescence detection is achieved using a 30-element Ge Canberra SSD.

The limit of dilution for an EXAFS analysis is found to be around 100/200 ppm for an element in a natural soil and is

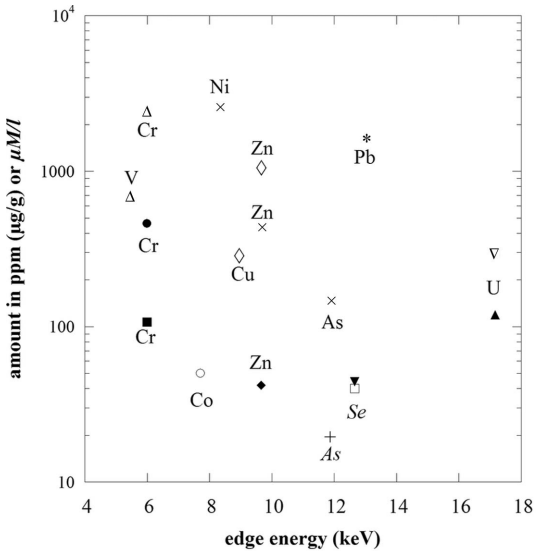

Figure 1
Concentration limits for XAS experiments performed on FAME in the biological (open symbols) and environmental (solid symbols) science fields as reported in the literature. The amounts correspond to μg g^{-1} (name of the element in bold) or μ*M* l^{-1} (italic). These experimental concentration limits are obtained during EXAFS studies except for the Se, V and two of the Cr experiments (Chaurand *et al.*, 2007; Rose, Cornu *et al.*, 2007; Gouget *et al.*, 2005; XANES studies). Open circles: Bakkaus *et al.* (2009) (vegetal). Open up-triangles: Chaurand *et al.* (2007) (slag). Open down-triangles: Carrière *et al.* (2006) (biological). Filled down-triangles: Collins *et al.* (2006) (soil). Filled circles: Doelsch *et al.* (2006) (soil). Filled up-triangles: Froideval *et al.* (2006) (Al hydroxide). Open squares: Gouget *et al.* (2005) (biological). Open diamonds: Kirpichtchikova *et al.* (2006) (soil). Filled diamonds: Manceau *et al.* (2005) (clay). Crosses (×): Manceau *et al.* (2007) (Fe–Mn coatings). Plus signs (+): Rose, Bergé-Lefranc *et al.* (2007) (biological). Filled squares: Rose, Cornu *et al.* (2007) (cement). Asterisks: Takahashi *et al.* (2007) (Fe–Mn oxides).

reduced for biological samples (down to 20 μmol l^{-1}). In some cases higher concentrations are also difficult to record. Two examples illustrate this limitation. At the V *K*-edge (Chaurand *et al.*, 2007) the XANES spectrum acquisition was mainly disturbed owing to the high contents of titanium (the Ti $K\beta$ and V $K\alpha$ fluorescence lines are superimposed) and calcium (the Ca $K\alpha$ fluorescence line saturates the detector). The problem is the same in an EXAFS study at the Ni *K*-edge (8.333 keV; Manceau *et al.*, 2007): the total amount of Ni is important (3300 ppm) but the counting ratio of the fluorescence detector is limited by the total amount of Mn and Fe. For experiments performed at higher energy, the efficiency of using appropriate filters to limit the effects of these fluorescence lines increases and the concentration limit reaches 119 ppm at the U L_{III}-edge (Froideval *et al.*, 2006).

3. Experimental details

3.1. Crystal analyser spectrometer

Johann's geometry (Johann, 1931) is used for the crystal analyser spectrometer (CAS). The analyzing plane is vertical: the bent crystal, the sample and the detector just above the sample are located on the Rowland circle (Fig. 2). Tests have

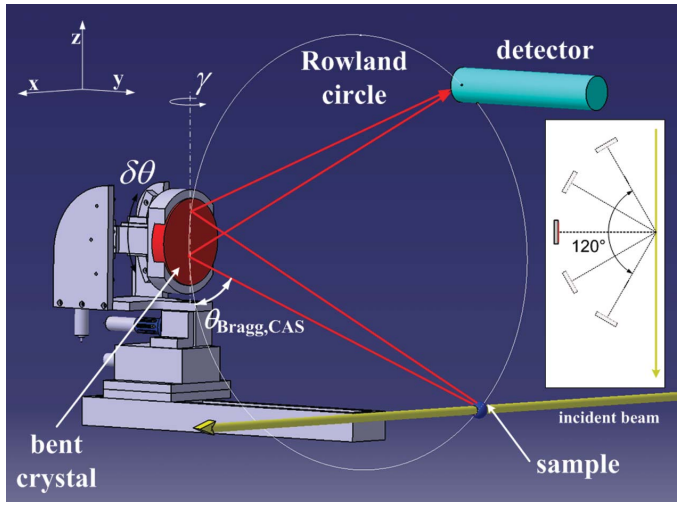

Figure 2
Schematic view of the set-up. The diffracting plane (*y*, *z*) containing the Rowland circle is vertical, normal to the horizontal incident beam (the angular domain covered by this single crystal ranges from 84 to 96° with respect to the incident X-rays). The energy selectivity is performed with two linear motions along the *y* and *z* axes which allow the $\theta_{Bragg,CAS}$ angle to be changed keeping the bent crystal on the Rowland circle. The two angular motions, γ and $\delta\theta$, allow a precise alignment of the crystal (position with respect to the *y* axis and verticality). Inset: schematic drawing of the crystal analyzer positioning.

been performed using a Si(111) spherical crystal (0.1 m in diameter) with a 0.5 m radius of curvature (ρ). The curvature radius of the crystal is twice the radius of the Rowland circle. Diffracted photons are focused on a NaI scintillation counter detector. All the different motions are achieved using standard linear and rotation motorized stages. The aim of the rotation stages is to make the bend crystal perfectly vertical ($\delta\theta$) and normal to the *y* axis (γ). The energy scans are performed only with the linear motions along the *y* and *z* axes. No goniometric system with large angular range is necessary in this vertical geometry. The spectrometer is then very simple, both from a geometrical and technological point of view.

The $\theta_{Bragg,CAS}$ angle ranges from 45 to 86°. Using four kinds of bent crystals, Si(331), Si(311), Si(111) and Si(110), this angular range allows photon energies ranging from 4 to 13.65 keV to be probed. Such an energy range is sufficient to probe the $K\alpha$ or $K\beta$ fluorescence line of all the elements from Ca [Z = 20, with the Si(311) reflection] to Rb [Z = 37, with the Si(555) reflection], and the $L\alpha$ or $L\beta$ fluorescence lines of all the elements from Te (Z = 52) to U (Z = 92). The probed scattering angle can be changed from 30 to 150° with respect to the incident beam (inset of Fig. 2). All the results presented in this manuscript have been obtained with a mean scattering angle of 90°.

The technology for the elaboration of this spherically bent Si single crystal has been developed for high-resolution purposes, below 200 meV (Collart *et al.*, 2005). For the present spectrometer two constraints are predominant. Firstly we need to increase the solid angle of analysis to increase the count rate, and secondly the spectrometer needs to be compact to fit into the available space on the beamline. For all of the

experiments presented in this paper the Si(444) reflection was chosen. Energy resolution measurements were also performed using the Si(333) reflection. Our aim is to approach a 1 eV resolution which is largely sufficient for the applications described.

3.2. Energy resolution

The total energy resolution of the spectrometer depends both on the incident beam characteristics (energy resolution of the monochromator, vertical width of the beam on the sample) and on the crystal analyser itself (intrinsic resolution of the crystal, imperfections of the crystal owing to the bending process, aberrations owing to the Johann's geometry). A detailed description of these different contributions is given by Collart *et al.* (2005). The analytical contributions of the incident beam characteristics are as follows.

The energy resolution of the incident beam depends mainly on the intrinsic resolution of the monochromator, owing to the good collimation of the incident white beam by the first mirror (Proux *et al.*, 2006),

$$\omega_{\rm Darwin} = \frac{2r_{\rm e}\lambda^2 C\left|F(hkl)\right|}{V\pi\sin\left(2\theta_{\rm Bragg}\right)}, \qquad (1)$$

where $r_{\rm e}$ (Å) is the classical electron radius, λ (Å) $\simeq 12.3984/E$ (keV) is the wavelength of the diffracted beam directly linked to the selected energy E, C is the polarization factor (equal to 1 in this case), $F(hkl)$ is the structure factor including the Debye–Waller factor, V (Å^3) is the unit-cell volume and $\theta_{\rm Bragg}$ is the Bragg angle of the monochromator.

The finite vertical size (h) of the incident beam on the sample leads to a decrease in the resolution of the CAS, which can be simply expressed by differentiating Bragg's law,

$$\Delta E_{\rm vertical\,size} = E\cot\left(\theta_{\rm Bragg,CAS}\right)\Delta\theta, \qquad (2)$$

where $\Delta\theta$ is the vertical angular size of the incident beam on the sample seen by the CAS and $\theta_{\rm Bragg,CAS}$ is the Bragg angle of the CAS. Owing to the order of magnitude of this vertical size with respect to the distance between the sample and the CAS (ρ), $\Delta\theta$ can be expressed in first approximation as h/ρ.

The total energy resolution of the CAS is characterized using the elastic peak of the incident beam measured for scattering angles ranging from 84 to 96° with respect to the incident beam. The CAS is tuned successively to the Cu $K\alpha_1$, Fe $K\alpha_1$ and Fe $K\beta_1$ energy (the energy, Bragg angle of the CAS and used Si reflection are gathered in the first lines of Table 1). The incident energy on the sample (water contained in a 3 mm-diameter glass capillary) is scanned around the analyser energy. The FWHM of the peak, fitted by a Gaussian curve, equals 1.4 eV for Cu $K\alpha_1$ (Fig. 3), 2.0 eV for Fe $K\alpha_1$ and 6.6 eV for Fe $K\beta_1$ (spectra not shown). For each experimental condition, $\omega_{\rm Darwin}$ [theoretical value, equation (1)] and $\Delta E_{\rm vertical\ size}$ (calculated from the h value, 200 µm) have been estimated (Table 1). Assuming a Gaussian shape for all the energy resolution components (Collart *et al.*, 2005; Huotari *et al.*, 2006), the total energy resolution can be expressed as follows,

Table 1
Contributions to the final resolution of the crystal analyser spectrometer.

	Cu $K\alpha_1$	Fe $K\alpha_1$	Fe $K\beta_1$
Emission (eV)	8047.78	6403.84	7057.98
$\theta_{\rm Bragg,CAS}$ (°)	79.313	67.945	57.185
Si reflection	(444)	(333)	(333)
Theoretical monochromator Darwin width, $\omega_{\rm Darwin}$ (eV)	0.4	0.37	0.37
Theoretical vertical source size, $\Delta E_{\rm vertical\ size}$ (eV)	0.6	1.0	1.8
Measured total energy resolution, $\Delta E_{\rm total}$ (eV)	1.4	2	6.6
Calculated† crystal analyser spectrometer resolution, $\Delta E_{\rm CAS}$ (eV)	1.2	1.7	6.3

† Calculated using equation (3): $\Delta E^2_{\rm CAS} = \Delta E^2_{\rm total} - \omega^2_{\rm Darwin} - \Delta E^2_{\rm vertical\,size}$.

$$\Delta E^2_{\rm total} = \omega^2_{\rm Darwin} + \Delta E^2_{\rm vertical\,size} + \Delta E^2_{\rm CAS}. \qquad (3)$$

One can then calculate the energy resolution of the CAS, $\Delta E_{\rm CAS}$, to around 1.2 eV for Cu $K\alpha_1$, 1.7 eV for Fe $K\alpha_1$ and 6.3 eV for Fe $K\beta_1$. These CAS energy resolutions are mostly due to the geometrical aberrations [Johann's geometry error which increases when the Bragg angle decreases; see, for example, Collart *et al.* (2005)] and defects of the CAS, the Darwin width of the crystal being very small for the used (333) and (444) reflections. Moreover, it should be noted that the total energy resolution depends on $\theta_{\rm Bragg,CAS}$ owing to the vertical beam size [equation (2)]. The resolution will be better for a $\theta_{\rm Bragg,CAS}$ value as close as possible to 90°. For the Cu $K\alpha_1$ and Fe $K\alpha_1$ fluorescence lines the obtained resolution is suitable for RIXS, inner-shell (Glatzel & Bergmann, 2005), resonant X-ray emission (RXES; Rueff *et al.*, 2004) and XRS (Bowron *et al.*, 2000) spectroscopies. For the Fe $K\beta_1$ fluores-

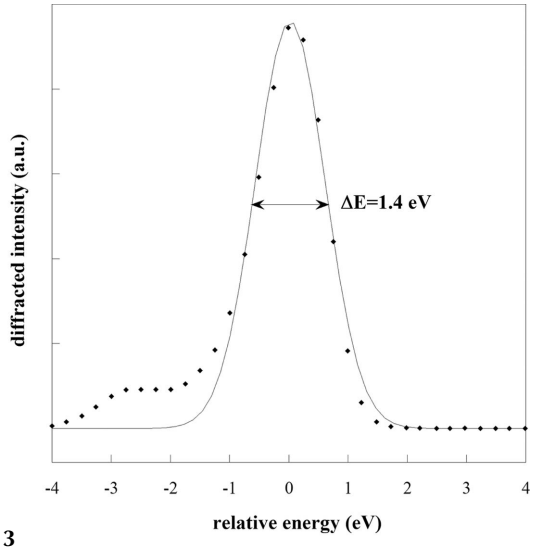

Figure 3
Energy scans for the elastic scattering signal from a water sample measured around 8047.78 eV (optimized energy, $E_{\rm opt}$, for the CAS) using the Si(444) bent crystal (R = 0.5 m) at 90° with respect to the incident beam expressed as a function of the relative energy ($E_{\rm opt} - E$). Solid diamonds: experimental points. Solid line: theoretical adjustment by a Gaussian function.

Table 2
Statistical parameters: effective number of counts ($N_{\rm eff}$), total counting time (T) and signal-to-noise ratio estimated from statistical and experimental considerations (see text).

Measurements	SSD (13 elements)	CAS
$N_{\rm eff}$ (s^{-1})	139000	75000
T (s) at 14 Å^{-1}	12	200
$(S/N)_{\rm stat}$ at k = 14 Å^{-1}	0.47	1.4
$(S/N)_{\rm exp}$ at k = 14 Å^{-1}	0.52	1.25

cence line the energy resolution might not be sufficient for inelastic experiments but suitable for XAS measurement.

4. Preliminary results

Different experiments were performed in order to check the ability to perform high-resolution spectroscopy experiments on a BM beamline. For each kind of experiment we checked (i) the reproducibility, (ii) the count rate and (iii) the resolution of the measurement in comparison either with 'standard' XAS measurements or measurements performed on other beamlines and reported in the literature.

4.1. XAS experiment

The merits of the CAS detector for measuring with better statistics a weak fluorescence signal out of an intense background signal were tested by measuring the signal from Cu impurities in goethite (α-FeOOH). The Cu/(Cu+Fe) mole fraction of the sample is 0.015, and above the Cu K-edge the integrated number of photons from the Cu $K\alpha$ fluorescence line is about two orders of magnitude lower than the total number of background photons from the Fe $K\alpha$ line [$I(\mathrm{Cu}\,K\alpha)/I(\mathrm{Fe}\,K\alpha) \simeq 0.02$] and the Compton scattering peak. Two EXAFS spectra were recorded, one by measuring the intensity of the Cu $K\alpha_{1+2}$ line with a standard 13-element Ge SSD and the other by measuring a fraction of the intensity of the Cu $K\alpha_1$ PFY with the CAS detector. In the first experiment, chromium filters were added between the sample and the SSD to attenuate the Fe $K\alpha_{1+2}$ peak relative to the Cu $K\alpha_{1+2}$ peak. Their thicknesses were optimized to maximize the effective number of counts ($N_{\rm eff}$), defined as the square of the signal-to-noise ratio,

$$N_{\rm eff} = \frac{N_{\rm S}^2}{N_{\rm S}+N_{\rm B}} = \frac{N_{\rm S}}{1+N_{\rm B}/N_{\rm S}}, \qquad (4)$$

with $N_{\rm S}$ the desired fluorescence photons (difference in the number of photons above and below the edge) and $N_{\rm B}$ the background signal in the Cu $K\alpha$ energy window (tails of the Fe $K\alpha$ and Compton scattering peaks, and fluorescence line induced by the filter). After optimization of the SSD and the associated filters, the effective number of counts was about 139000 s^{-1} ($N_{\rm B}$ = 12000 s^{-1}, $N_{\rm S}$ = 150000 s^{-1}) for the 13 elements. In the second experiment with the CAS, $N_{\rm eff} = N_{\rm S}$ = 75000 s^{-1} for the same storage-ring current as previously (200 mA). These values, $N_{\rm eff}$ and total counting time (T) for the two experiments, are gathered in Table 2.

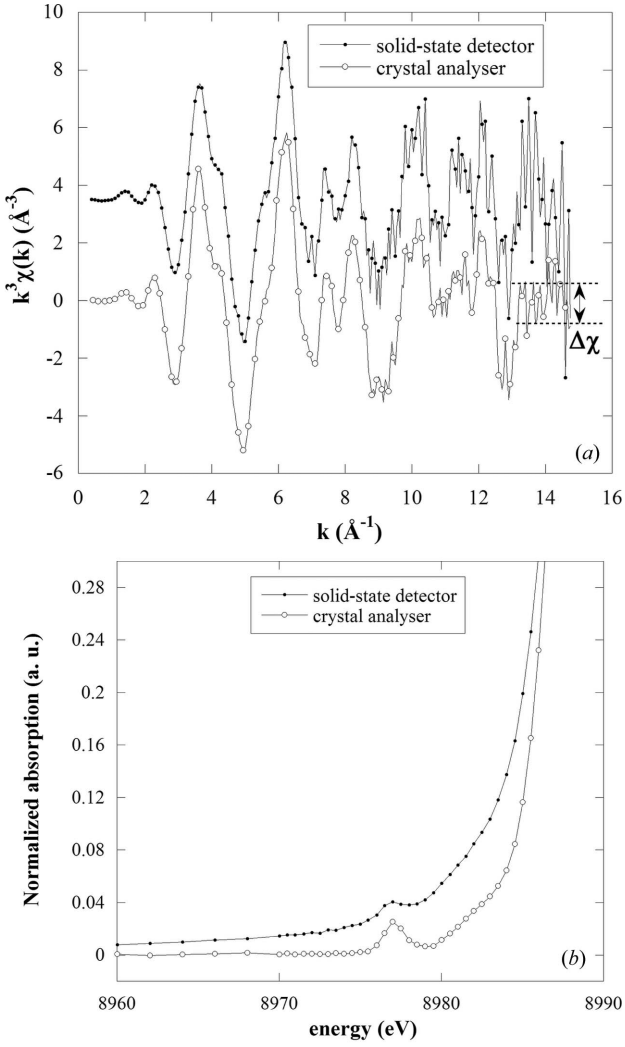

Figure 4
Comparison of k^3-weighted EXAFS (*a*) and pre-edge (*b*) Cu K-edge spectra for a pure α-FeO(OH) (goethite) containing copper (2000 ppm). Measurements were made in the fluorescence mode using a crystal analyser ($E_{\rm analyser} = E_{K\alpha_1}$, energy resolution = 1.4 eV) and 13-element Ge solid-state detector ($E_{\rm SSD} = E_{K\alpha_{1+2}}$, energy resolution = 300 eV). $\Delta\chi$: experimental points distribution used for the signal-to-noise ratio determination.

The two EXAFS spectra are shown in Fig. 4(*a*). As expected from statistics [$T_{\rm CAS}N_{\rm eff}({\rm CAS}) > T_{\rm SSD}N_{\rm eff}({\rm SSD})$] the CAS spectrum has a higher signal-to-noise (S/N) ratio. A rough experimental quantification of the noise can be carried out by considering the half of the amplitude of the experimental points distribution, $\Delta\chi$, on the normalized data. The EXAFS wiggle at k = 14 Å^{-1} has a noise of about 1.9 with the SSD, and about 0.8 with the CAS. This is a significant improvement in comparison with the earlier measurement with a 12-element Si SSD on the ultra-diluted sample ID26 beamline at the ESRF (Manceau *et al.*, 2000). At this time the EXAFS spectrum of this sample could not be measured with good enough statistics up to k = 14 Å^{-1} for a quantitative analysis.

From the $N_{\rm eff}$ and T of a given spectrum it is possible to calculate the statistical S/N ratio of the normalized data (edge jump equal to 1), $(S/N)_{\rm stat}$. The modulations of the normalized

EXAFS signal, $\chi(k)$, are here weighted by k^3. The statistical signal $[k^3\chi(k)]$ to noise ratio is then expressed as

$$(\mathrm{S/N})_{\mathrm{stat}} = (TN_{\mathrm{eff}})^{1/2}/k^3. \quad (5)$$

The experimental noise has been estimated as half of the experimental point distribution, $\Delta\chi$ (Fig. 4*a*). In the high k-range the amplitude of the EXAFS wiggles becomes low, and the normalized signal is close to unity. The experimental signal-to-noise ratio, $(\mathrm{S/N})_{\mathrm{exp}}$, can then be expressed as

$$(\mathrm{S/N})_{\mathrm{exp}} = \frac{1}{2\Delta\chi}. \quad (6)$$

The statistical and experimental signal-to-noise ratios obtained by the two different measurements are gathered in Table 2. In both cases, $(\mathrm{S/N})_{\mathrm{exp}} \simeq (\mathrm{S/N})_{\mathrm{stat}}$, showing that the data quality is limited by the counting statistics.

XANES spectra were also recorded using the two detectors (Fig. 4*b*) in order to illustrate how the use of CAS with a high energy resolution allows spectra to be acquired with improved resolution. The XANES spectrum measured using the CAS has a clear improved resolution compared with the SSD measurement, especially the 1*s* to 3*d* pre-edge feature at 8977 eV (Fig. 4*b*). However, it should be noted that this improvement can be affected by strong resonant effects. Fluorescence analysis is achieved at a constant energy (in the EXAFS region), but the energy position of the fluorescence line is no longer constant close to this edge. The so-obtained XANES spectra have to be analyzed with great care.

XAS measurements can therefore be performed easily with a bent-crystal analyser spectrometer, even with an energy resolution smaller than the natural width of the analyzed fluorescence line. This fact demonstrates the excellent stability of the overall spectrometer. By taking advantage of the high-energy-resolution fluorescence detection it is possible to perform an EXAFS acquisition with a good S/N ratio irrespective of the nature of the matrix and with an improved resolution of the pre-edge and edge features. This is of crucial importance, especially in the environmental and geochemistry sciences fields. For example, when the probed fluorescence line is in the same energy range as lines of another element in the matrix, the use of selective filters is then inefficient. With this spectrometer the detection limit is completely independent of the nature of the matrix. One can then expect to perform XAS experiments in the environmental science field where the matrix is heavy on elements with the same dilution as those obtained in the biological science fields (light matrix) (Fig. 1), *i.e.* close to 20 ppm with the 30-element solid-state detector. For this purpose a CAS including five bent crystals is currently under construction. The number of collected photons will be identical in the two systems, without any problem of saturation with the CAS.

Moreover, when the sample is optically thin, it has been shown that high-resolution fluorescence detection allows the energy range for EXAFS analysis to extend beyond other absorption edges (Glatzel *et al.*, 2005). The thickness limitation, which is the standard requirement for conventional fluorescence-detected absorption spectroscopy, can be obtained in some particular case by diluting the sample. However, this dilution procedure cannot be easily applied to most samples where (i) the probed element is already diluted and (ii) the extension of the energy range is often limited by the absorption edges of the main components of the matrix. As an example, we acquired the PFY-EXAFS spectra of copper ions ([Cu] = 0.1 mol l^{-1}) in aqueous solution containing zinc ions ([Zn] = 0.5 mol l^{-1}) by measuring the Cu $K\alpha_1$ line (Fig. 5). The sample was thick, contained in a 3 mm-diameter quartz capillary. The drop in the Cu *K*-edge EXAFS spectrum corresponds to the increase in the total absorption cross section of the sample owing to the Zn *K*-edge, which leads to a decrease of the incident photon beam intensity at a given depth in the sample.

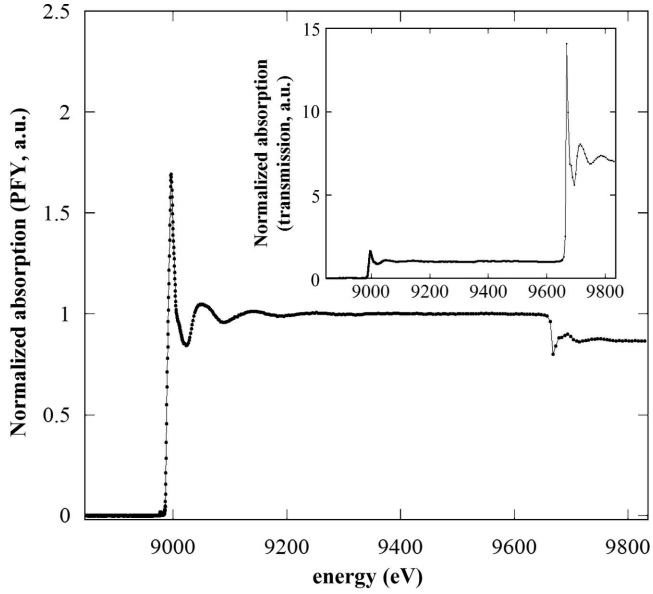

Figure 5
PFY-EXAFS Cu *K*-edge spectrum of copper aqueous solution ([Cu] = 0.1 mol l^{-1}) containing zinc ions ([Zn] = 0.5 mol l^{-1}) in a 3 mm glass capillary. Inset: simultaneous measurement of the absorption edges in the transmission mode. Spectra were normalized for a Cu *K*-edge jump of 1.

4.2. Resonant inelastic X-ray scattering experiment

RIXS is a powerful tool for the study of electronic states in solids, giving access to site, element and orbital selective information (Kotani & Shin, 2001). RIXS spectra probe the unoccupied local and partial density of states of the probed element. This experiment was performed on a CuO sample; this compound has already been studied by this technique (Hayashi *et al.*, 2002, 2003; Döring *et al.*, 2004).

In our sample the copper weight concentration reaches 1% after dilution of pure CuO compound with boron nitride powder. The count rate was around 56000 s^{-1} at the peak maximum of Cu $K\alpha_1$ and 32000 s^{-1} at the peak maximum of Cu $K\alpha_2$, for an excitation energy of 8989 eV. Acquisition was performed by scanning the scattered energy (emission energy; energy step: 0.25 eV) for different incident energies (excitation energy; energy step: 0.5 eV). The emission energy ranges from 8010 to 8060 eV to cover both $K\alpha_2$ (1*s* to $2p_{1/2}$ transition)

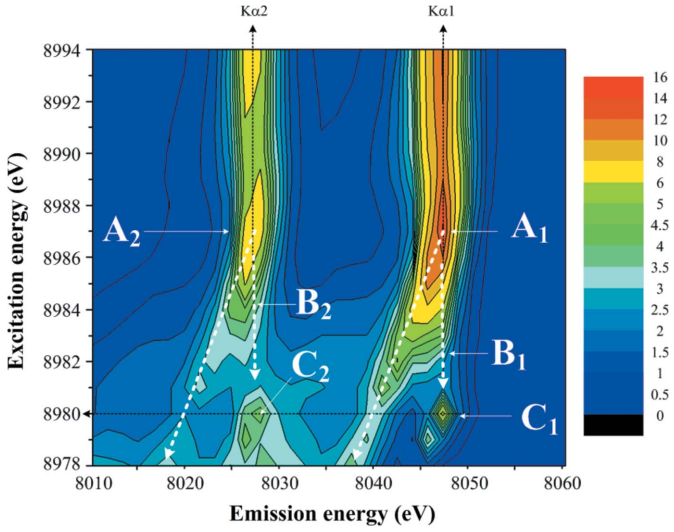

Figure 6
Contour maps of the 1*s*2*p* RIXS plane of CuO near the Cu absorption *K*-edge. The intensity is normalized to the incident photon beam intensity.

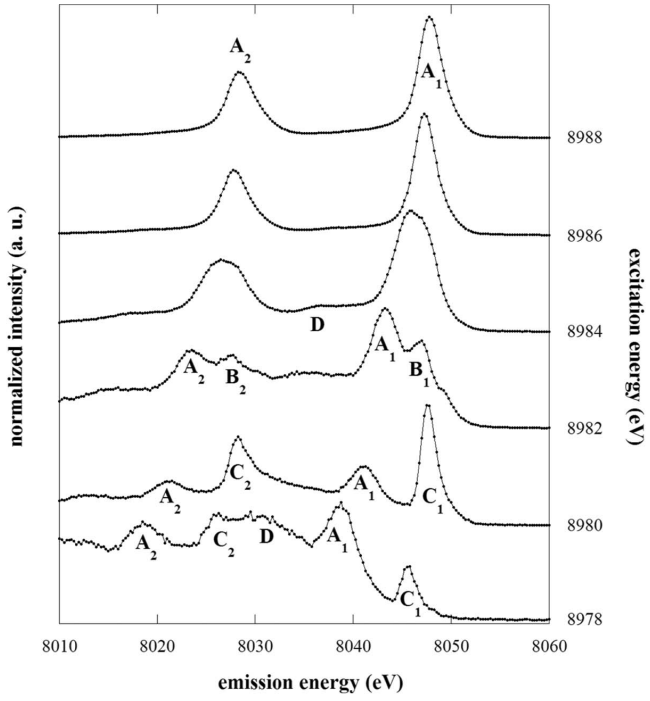

Figure 7
Emission spectra of CuO as a function of the excitation energy. Each spectrum is normalized to its maximum value.

and $K\alpha_1$ (1*s* to $2p_{3/2}$ transition) emission lines. A two-dimensional map of the RIXS spectrum was reconstructed from the series of emission spectra and colour interpolated. Detail of this mapping is shown in Fig. 6, which focuses on the pre-edge area. Several emission spectra obtained for different excitation energies are presented in Fig. 7. The obtained RIXS and emission spectra are comparable with those reported in the literature (Hayashi *et al.*, 2002, 2003; Döring *et al.*, 2004; Welter *et al.*, 2005) in terms of signal-to-noise ratio and resolution of the features. The peaks, *i.e.* the electronic transitions

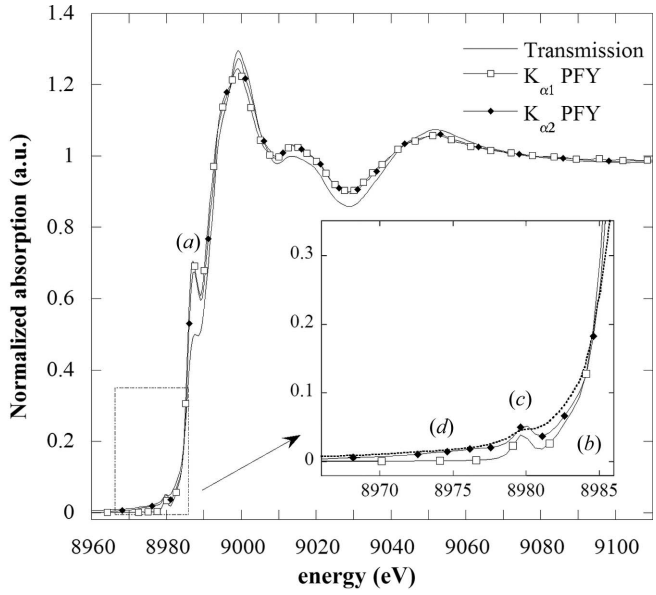

Figure 8
Partial fluorescence yield XANES spectra of CuO compared with a conventional spectrum obtained in transmission mode. Inset: detail of the pre-edge features. For details of the (*a*), (*b*), (*c*) and (*d*) features, see text.

which occur, have been discussed and we recall here the main results.

The Cu $K\alpha_1$ and $K\alpha_2$ fluorescence lines are clearly observable above the absorption edge. As the excitation energy decreases, two features appear, labelled A_1 and A_2, originating from the $K\alpha_1$ and $K\alpha_2$ transitions, respectively. The positions of these features shift to lower energy when the excitation energy decreases, the transferred energy being constant. Two other features labelled B_1 and B_2 appear at lower energy, distinguishable shoulders at 8984 eV, clearly distinct at 8982 eV and no longer visible at 8980 eV. These peaks are attributed to 'shake-up' valence excitations, induced by Coulomb interaction of the 1*s* hole with the Cu 3*d* system (Döring *et al.*, 2004). Another set of two peaks, C_1 and C_2, appear at 8982 eV. A rigorous interpretation of similar features in La_2CuO_4 has been given by Shukla *et al.* (2006). These features are due to quadrupolar excitation to the narrow 3*d* level. Finally, a broad peak labelled D (Fig. 7) can be distinguished between the A_1 and A_2 peaks. The position of this very large feature shifts to low energy when the excitation energy decreases.

XAS acquisitions were performed with the CAS on this CuO pellet. The PFY XANES spectra obtained with the CAS optimized at the Cu $K\alpha_1$ and Cu $K\alpha_2$ energies are shown in Fig. 8, superimposed with the transmission spectra for comparison. As for Fig. 4(*b*), each feature is better resolved in the PFY spectra with respect to the standard transmission XAS spectrum: the edge feature (*a*) and the 1*s* to 3*d* band (*c*). In the low energy range, below 8977 eV, and for the $K\alpha_1$ PFY XANES, the normalized absorption is close to zero. For the $K\alpha_2$ PFY XANES and transmission XAS spectra the absorption is slightly but unambiguously higher (0.017 at 8975 eV). This absorption increase is due to the existence of the broad D band: its contribution is taken into account in the

transmission spectrum, in the $K\alpha_2$ PFY-XANES but not in that for $K\alpha_1$.

Owing to the sharpening effect of the resonant process, pre-edge and edge features can be observed with a resolution better than the 1*s* core-hole lifetime in a PFY measurement (Hämäläinen *et al.*, 1991). Moreover, acquisition of the detailed emission spectra for various incident energies allows the origin of these features to be elucidated (Rueff *et al.*, 2004).

4.3. X-ray Raman scattering experiment

X-ray Raman scattering is the X-ray energy-loss version of XAS. In such an experiment the hard X-ray incident photon is inelastically scattered (Compton scattering) and a fraction of its energy is transferred to the sample through electronic transitions. By measuring the inelastic spectrum in the energy-transfer range corresponding to an absorption edge, the core-hole level probes the available states in the same way as the photoelectron in XANES and EXAFS. So the same XAS features are seen in the Compton scattering when the energy transfer equals the binding energy of the probed element (see, for example, Schükle *et al.*, 1986; Bergmann, Glatzel & Cramer, 2002). The use of hard X-rays with a large penetrating power allows low-energy edges of elements in environments which cannot be studied using soft X-rays (high-pressure and high-temperature environments typically; Wernet *et al.*, 2005) to be probed even if the cross section of such a process is very weak compared with the photo-absorption process.

The aims of these measurements were to test the stability of the set-up over a long time (the acquisitions were performed during more than one day) and to evaluate whether the flux on the sample is sufficient.

The oxygen *K*-edge of pure water has been obtained with a resolution of 1.4 eV by XRS at 8 keV. A similar measurement had been previously performed on undulator beamlines at the ESRF (ID28) and APS (BioCAT 18ID) with 2 eV (Bowron *et al.*, 2000) and 1 eV (Bergmann, Wernet *et al.*, 2002) resolutions, respectively. The inelastic scattering signal was observed with scattering angles between 84 and 96°. The energy transfer was scanned through the oxygen *K*-edge by changing the incident energy on the sample from 8560 to 8720 eV, the analysed energy being fixed (8058 eV). A helium bag was used to limit air absorption on the source-to-crystal and crystal-to-detector X-ray paths. The number of counts changed then from $\sim$50 s^{-1} (before the O *K*-edge, at 530 eV) to $\sim$115 s^{-1} (at the maximum of the XANES, at 540 eV) and $\sim$75 s^{-1} (after the edge, at 550 eV). Thirty spectra were recorded and summed. The acquisition time corresponded to 180 s point^{-1}, *i.e.* a total acquisition time of 30 h. The obtained spectra are shown in Fig. 9, for the XANES (Fig. 9*a*) and EXAFS up to 6 Å^{-1} (Fig. 9*b*). The carbon *K*-edge of glassy carbon was obtained under the same experimental conditions, with a total resolution of 1.7 eV at 8051 eV and scattering angles between 139 and 151°. The XANES spectrum obtained is shown in Fig. 10 with the quasi-elastic peak in inset.

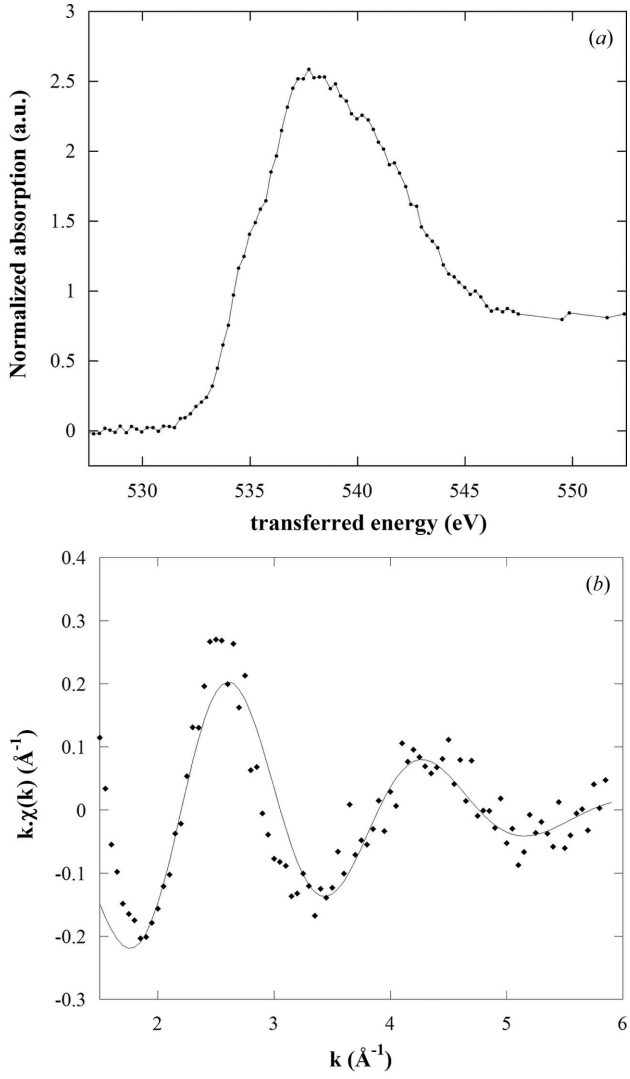

Figure 9
Oxygen *K* absorption edge measured by X-ray Raman scattering for liquid water under ambient conditions: (*a*) XANES and (*b*) EXAFS spectra. The profile of the elastic peak is shown in Fig. 3.

The quality and resolution of the O *K*-edge XANES spectrum of water can be compared with the spectra already obtained (Bowron *et al.*, 2000; Bergmann, Wernet *et al.*, 2002). The feature in the edge at 535 eV is clearly distinguished even though not as marked as in the 1 eV resolution spectrum (Bergmann, Wernet *et al.*, 2002). Interpretation of those spectra has been proposed but is still controversial (Wernet *et al.*, 2004; Prendergast & Galli, 2006). The EXAFS signal (Fig. 9*b*) presents a single oscillation frequency characteristic of the O—O bond. A simple analysis using the *Feff* code (Rehr & Albers, 2000) was performed. The fit is consistent with a first oxygen–oxygen bond length at a value of 2.89 Å, in agreement with the 2.87 Å value found by the same technique (Bowron *et al.*, 2000), especially when one considers the statistical dispersion of the experimental points.

The carbon *K*-edge of glassy carbon is shown in Fig. 10. This XANES spectrum exhibits characteristic features around 286 eV and 293 eV. These transitions are very sensitive to the

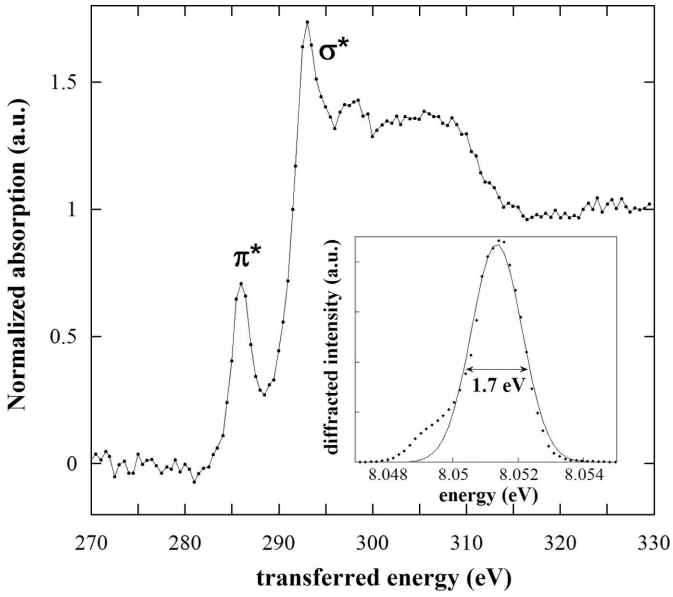

Figure 10
Carbon *K*-edge measured by X-ray Raman scattering for glassy carbon. Inset: profile of the elastic peak.

degree of unsaturation and to the carbon–neighbour bond lengths (Bergmann *et al.*, 2000). One can compare the spectrum measured here with those obtained with a better resolution, by XRS (1 eV) and electron yield (0.15 eV), on graphite (Bergmann, Glatzel & Cramer, 2002). The different spectral features are still well marked, the pre-edge (1*s* to π^*), the white line (1*s* to σ^*) and the small peak around 298 eV. However, the two small peaks at ∼304 and ∼308 eV, clearly visible in the electron yield measurement, and partially in the 1 eV resolution XRS measurement, are damped and merged in our 1.7 eV XRS measurement.

This technique is really promising for the XAS study of light elements in absorbing environments (Krisch & Sette, 2002), from simple experiments such as glass capillaries to complicated ones using high-pressure high-temperature devices (Wernet *et al.*, 2005). Moreover, compared with experiments performed using soft X-rays, XRS allows the bulk part of the sample to be studied, not only its near surface (Bergmann, Glatzel & Cramer, 2002).

5. Conclusion

A high-energy resolution crystal analyzer spectrometer, with a bending radius of 0.5 m, has been commissioned on CRG-FAME. The feasibility of the different types of experiments has been demonstrated, including X-ray absorption spectroscopy, resonant inelastic X-ray scattering and X-ray Raman scattering experiments. All these experiments show the very good stability of the set-up, both the beamline optics and the spectrometer, even for very long acquisition times. The use of such a simple device on a classic bending-magnet beamline allows an improvement of the quality of spectra: EXAFS on a diluted element independently of the nature of the matrix and XANES with an improved resolution being the major motivation. Moreover, new spectroscopic techniques can now be performed, to probe the various electronic transitions occurring during the absorption process (RIXS) or to perform an XAS-like experiment of a light element using hard X-rays (XRS). One of the current limitations is the solid angle of detection and thus the statistics of the measurement: a spectrometer including five bent crystals has been designed and is now under construction to improve this point.

The authors wish to acknowledge Jean-François Bérard and Stefan Arnaud from the CRG-D2AM beamline for the loan of the NaI scintillation detector, the ESRF detector pool for the loan of the corresponding processing module, Wouter Van Beek and Herman Emerich from the CRG-SNBL beamline for the loan of a 13-element Ge SSD, and Julianne James-Smith and Perrine Chaurand for their assistance in manuscript preparation.

References

Arcovito, A., Lamb Don, C., Nienhaus, G. U., Hazemann, J.-L., Benfatto, M. & Della Longa, S. (2005). *Biophys. J.* **88**, 2954–2964.
Bakkaus, E., Carrière, M., Collins, R. N., Khodja, H., Proux, O., Morel, J.-L. & Gouget, B. (2009). To be published.
Bergmann, U. & Cramer, S. P. (1998). *Proc. SPIE*, **3448**, 198–209.
Bergmann, U., Glatzel, P. & Cramer, S. P. (2002). *Microchem. J.* **71**, 221–230.
Bergmann, U., Mullins, O. C. & Cramer, S. P. (2000). *Anal. Chem.* **72**, 2609–2612.
Bergmann, U., Wernet, Ph., Glatzel, P., Cavalleri, M., Pettersson, L. G. M., Nilsson, A. & Cramer, S. P. (2002). *Phys. Rev. B*, **66**, 092107.
Bowron, D. T., Krisch, M. H., Barnes, A. C., Finney, J. L., Kaprolat, A. & Lorenzen, M. (2000). *Phys. Rev. B*, **62**, R9223–R9227.
Carrière, M., Thiebault, C., Milgram, S., Proux, O. & Gouget, B. (2006). *Chem. Res. Toxicol.* **19**, 1637–1642.
Chaurand, P., Rose, J., Briois, V., Salome, M., Proux, O., Nassif, V., Olivi, L., Susini, J., Hazemann, J.-L., Domas, J., Chateau, L. & Bottero, J.-Y. (2007). *J. Phys. Chem. B*, **111**, 5101–5110.
Collart, E., Shukla, A., Gélébart, F., Morand, M., Malgrange, C., Bardou, N., Madouri, A. & Pelouard, J.-L. (2005). *J. Synchrotron Rad.* **12**, 473–478.
Collins, R. N., Tran, N. D., Bakkaus, E., Avoscan, L. & Gouget, B. (2006). *Environ. Sci. Technol.* **40**, 7778–7783.
D'Angelo, P., Pacello, F., Mancini, G., Proux, O., Hazemann, J.-L., Desideri, A. & Battistoni, A. (2005). *Biochemistry*, **44**, 13144–13150.
Doelsch, E., Basile-Doelsch, I., Rose, J., Masion, A., Borschneck, D., Saint Macary, H. & Bottero, J.-Y. (2006). *Environ. Sci. Technol.* **40**, 7602–7608.
Döring, G., Sternemann, C., Kaprolat, A., Mattila, A., Hämäläinen, K. & Schülk, W. (2004). *Phys. Rev. B*, **70**, 085115.
Froideval, A., Del Nero, M., Gaillard, C., Barillon, R., Rossini, I. & Hazemann, J.-L. (2006). *Geochim. Cosmochim. Acta*, **70**, 5270–5284.
Glatzel, P. & Bergmann, U. (2005). *Coordin. Chem. Rev.* **249**, 65–95.
Glatzel, P., de Groot, F. M. F., Manoilova, O., Grandjean, D., Weckhuysen, B. M., Bergmann, U. & Barrea, R. (2005). *Phys. Rev. B*, **72**, 014117.
Gouget, B., Avoscan, L., Sarret, G., Collins, R. & Carrière, M. (2005). *Radiochim. Acta*, **93**, 683–690.

Goulon, J. *et al.* (2005). *J Synchrotron Rad.* **12**, 57–69.
Hämäläinen, K., Siddons, D. P., Hastings, J. B. & Berman, L. E. (1991). *Phys. Rev. Lett.* **67**, 2850–2853.
Hayashi, H., Takeda, R., Udagawa, Y., Nakamura, T., Miyagawa, H., Shoji, H., Nanao, S. & Kawamura, N. (2003). *Phys. Rev. B*, **68**, 045122.
Hayashi, H., Udagawa, Y., Caliebe, W. A. & Kao, C.-C. (2002). *Phys. Rev. B*, **66**, 033105.
Hazemann, J. L., Nayouf, K. & de Bergevin, F. (1995). *Nucl. Instrum. Methods Phys. Res. B*, **97**, 547–550.
Huotari, S., Albergamo, F., Vankó, Gy., Verbeni, R. & Monaco, G. (2006). *Rev. Sci. Instrum.* **77**, 053102.
Johann, H. H. (1931). *Z. Phys.* **69**, 185–206.
Khelashvili, G., Ivanov, I., Morrison, T. I., Bunker, G. & Chapman, D. (2002). *Rev. Sci. Instrum.* **73**, 1534–1536.
Kirpichtchikova, T., Manceau, A., Spadini, L., Panfili, F., Marcus, M. & Jacquet, T. (2006). *Geochim. Cosmochim. Acta*, **70**, 2163–2190.
Kotani, A. & Shin, S. (2001). *Rev. Mod. Phys.* **73**, 203–246.
Krisch, M. & Sette, F. (2002). *Surf. Rev. Lett.* **9**, 969–976.
Kropf, A. J., Fortner, J. A., Finch, R. J., Cunnane, J. C. & Karanfil, C. (2005). *Phys Scr.* **115**, 918.
Manceau, A., Lanson, M. & Geoffroy, N. (2007). *Geochim. Cosmochim. Acta*, **71**, 95–128.
Manceau, A., Schlegel, M., Musso, M., Sole, V. A., Gauthier, C., Petit, P. E. & Trolard, F. (2000). *Geochim. Cosmochim. Acta*, **64**, 3643–3661.
Manceau, A., Tommaseo, C., Rihs, S., Geoffroy, N., Chateigner, D., Schlegel, M. & Tisserand, D. (2005). *Geochim. Cosmochim. Acta*, **69**, 4007–4034.
Oyanagi, H., Tsukada, A., Naito, M., Saini, N. L., Lampert, M.-O., Gutknecht, D., Dressler, P., Ogawa, S., Kasai, K., Mohamed, S. & Fukano, A. (2006). *J. Synchrotron Rad.* **13**, 314–320.
Prendergast, D. & Galli, G. (2006). *Phys. Rev. Lett.* **96**, 215502.
Proux, O. *et al.* (2005). *Phys. Scr.* **115**, 970–973.
Proux, O., Nassif, V., Prat, A., Ulrich, O., Lahera, E., Biquard, X., Menthonnex, J.-J. & Hazemann, J.-L. (2006). *J. Synchrotron Rad.* **13**, 59–68.
Rehr, J. J. & Albers, R. C. (2000). *Rev. Mod. Phys.* **72**, 621–654.
Rose, J., Bergé-Lefranc, J.-L., Bellon, L., Orsiere, T., Hazemann, J.-L., Proux, O., Bottero, J.-Y. & Botta, A. (2007). ESRF Experimental Report 30.02.667. ESRF, Grenoble, France.
Rose, J., Cornu, S., Cousin, S., Benard, A., Deschatrettes, V., Hazemann, J.-L., Proux, O., Masion, A. & Grauby, O. (2007). ESRF Experimental Report 30.02.17. ESRF, Grenoble, France.
Rueff, J.-P., Journel, L., Petit, P.-E. & Farges, F. (2004). *Phys. Rev. B*, **69**, 235107.
Schülke, W. (2007). *Electron Dynamics by Inelastic X-ray Scattering, Series on Synchrotron Radiation*, Vol. 7, edited by J. Chikawa, J. R. Helliwell & S. W. Lovesey. Oxford: Oxford Science.
Schükle, W., Nagasawa, H., Mourikis, S. & Lanzki, P. (1986). *Phys. Rev. B*, **33**, 6744.
Shukla, A., Calandra, M., Taguchi, M., Kotani, A., Vankó, G. & Cheong, S.-W. (2006). *Phys. Rev. Lett.* **96**, 077006.
Takahashi, Y., Manceau, A., Marcus, M. A. & Usui, A. (2007). *Geochim. Cosmochim. Acta*, **71**, 984–1008.
Titov, A., Biquard, X., Halley, D., Kuroda, S., Bellet-Amalric, E., Mariette, H., Cibert, J., Merad, A. E., Merad, G., Kanoun, M. B., Kulatov, E. & Uspenskii, Yu. A. (2005). *Phys. Rev. B*, **72**, 115209.
Welter, E., Machek, P., Dräger, G., Brüggmann, U. & Fröba, M. (2005). *J. Synchrotron Rad.* **12**, 448–454.
Wernet, Ph., Nordlund, D., Bergmann, U., Cavalleri, M., Odelius, M., Ogasawara, H., Näslund, L. Å., Hirsch, T. K., Ojamäe, L., Glatzel, P., Pettersson, L. G. M. & Nilsson, A. (2004). *Science*, **304**, 995–999.
Wernet, Ph., Testemale, D., Hazemann, J.-L., Argoud, R., Glatzel, P., Pettersson, L. G. M., Nilsson, A. & Bergmann, U. (2005). *J. Chem. Phys.* **123**, 154503.
Zhong, Z., Chapman, L. D., Bunker, B. A., Bunker, G., Fischetti, R. & Segre, C. U. (1999). *J. Synchrotron Rad.* **6**, 212–214.